Supplementary Material

Preferred WMSA catalytic mechanism of the nucleotidyl transfer reaction in human DNA polymerase κ elucidates error-free bypass of a bulky DNA lesion

Lee Lior-Hoffmann[1], Lihua Wang[2], Shenglong Wang[1], Nicholas E. Geacintov[1], Suse Broyde[2] and Yingkai Zhang[1]

Department of Chemistry[1], Department of Biology[2], New York University, 100 Washington Square East, New York, NY 10003, USA

COMPUTATIONAL DETAILS:

Structure Preparation

The ternary crystal structure (PDB ID: 2OH2 (46)) of Pol κ_{19-526} with DNA and incoming dTTP (32) was the basis for our prepared enzyme-substrate model. However, this crystal structure contained a dideoxy terminus, lacking the 3'OH; in addition it contained the nucleotide binding Mg^{+2} ion but not the catalytic one. Furthermore, within the palm domain 57 residues (residues 225-281) were not resolved in the crystal structure. We were guided by our earlier modeling of the Pol κ active site (30) which was based on a Dpo4 crystal structure containing the O3'H (65) and the high resolution structure of Pol β containing a well-organized active site (34), to model an initial Pol κ structure for the present QM/MM-MD investigation. Since the critical O3'H group was dideoxy in the crystal structure to prevent reaction during the crystallization, the hydrogen on the primer dideoxyribose was replaced by O3'H. The nucleotide binding ion (Mg^{+2} B), was already present in the structure, but the missing catalytic ion (Mg^{+2} A) was modeled to create the conserved octahedral coordination. Missing residues 225 to 281 are in a flexible loop on the enzyme surface (89), far from the active site (>20Å, which is out of the QM/MM region, see below). To avoid the uncertainty introduced by modeling explicitly these missing residues, we simply treated the amino acid residues 224 and 282 as terminal residues. The A of the templating base and the T of the incoming dTTP were replaced with a G and a dCTP, to permit studies with the guanine lesion. We utilized the Leap module in AMBER 9 (47) to add missing hydrogen atoms. The protonation states of charged residues were determined by the H++ (90,91) and pdb2pqr (92) methods. When the two methods disagreed, protonation states were assigned based on the following criteria: the potential H-bonding network , solvent exposure of the ionizable residues, potential steric clashes if the proton was added, and preservation of the crystal structure.

MD computation protocol

The starting model was subjected to minimization of the hydrogens that were added by the LEAP module of the Amber 9 simulation package (47) with 600 steps of steepest descent and then an additional 600 steps of conjugate gradient minimization. A distance dependent dielectric function ($1/r^2$) was employed with dielectric constant 4.0. Using the SIMULAID program (93) the minimized system's orientation was optimized into a rectangular periodic box; then using the Amber LEAP module it was neutralized with 10 Na^+ counterions and was solvated with explicit TIP3P water (54); the periodic box had a 10.0 Å buffer around the enzyme-substrate complex. The subsequent energy minimizations and MD simulations were performed with the Particle-Mesh Ewald (98,99) method with 9.0 Å cutoff for the non-bonded interactions. In the MD simulations a time step of 2fs and the SHAKE algorithm (100) were used. The Berendsen coupling algorithm (97) with a 1.0 ps coupling parameter regulated the temperature, and the

pressure was maintained using isotropic position scaling. The solvent and the counterions were minimized first with 2500 steps of steepest descent minimization followed by 2500 cycles of conjugate gradient minimization; a force constant of 50 kcal·mol^{-1}·Å^{-2} was applied to restrain the protein, the DNA including the incoming dCTP and the Mg^{+2} ions. While gradually reducing this restraint to 25 kcal·mol^{-1}·Å^{-2} the solvent and counterions were further equilibrated over 30 ps MD at constant pressure and constant temperature of 10K. Next, the system was heated up to 310K with 80ps MD simulations at constant volume and was held at this temperature over additional 20ps of MD simulations under the same conditions. During the heating the restraint on the solute was released to 10 kcal·mol^{-1}·Å^{-2}. Then 30ps NPT MD simulation was performed to equilibrate the system with a looser coupling to the heat bath using a constant of 4 ps. The force constant on the solute was released again in two steps: first to 1 kcal·mol^{-1}·Å^{-2} with 40ps NPT MD simulations, and then to 0.1 kcal·mol^{-1}·Å^{-2} with 50 ps NPT MD simulations. Finally, a 3 ns production was conducted at a temperature of 310 K and a constant pressure of 1 Atm.

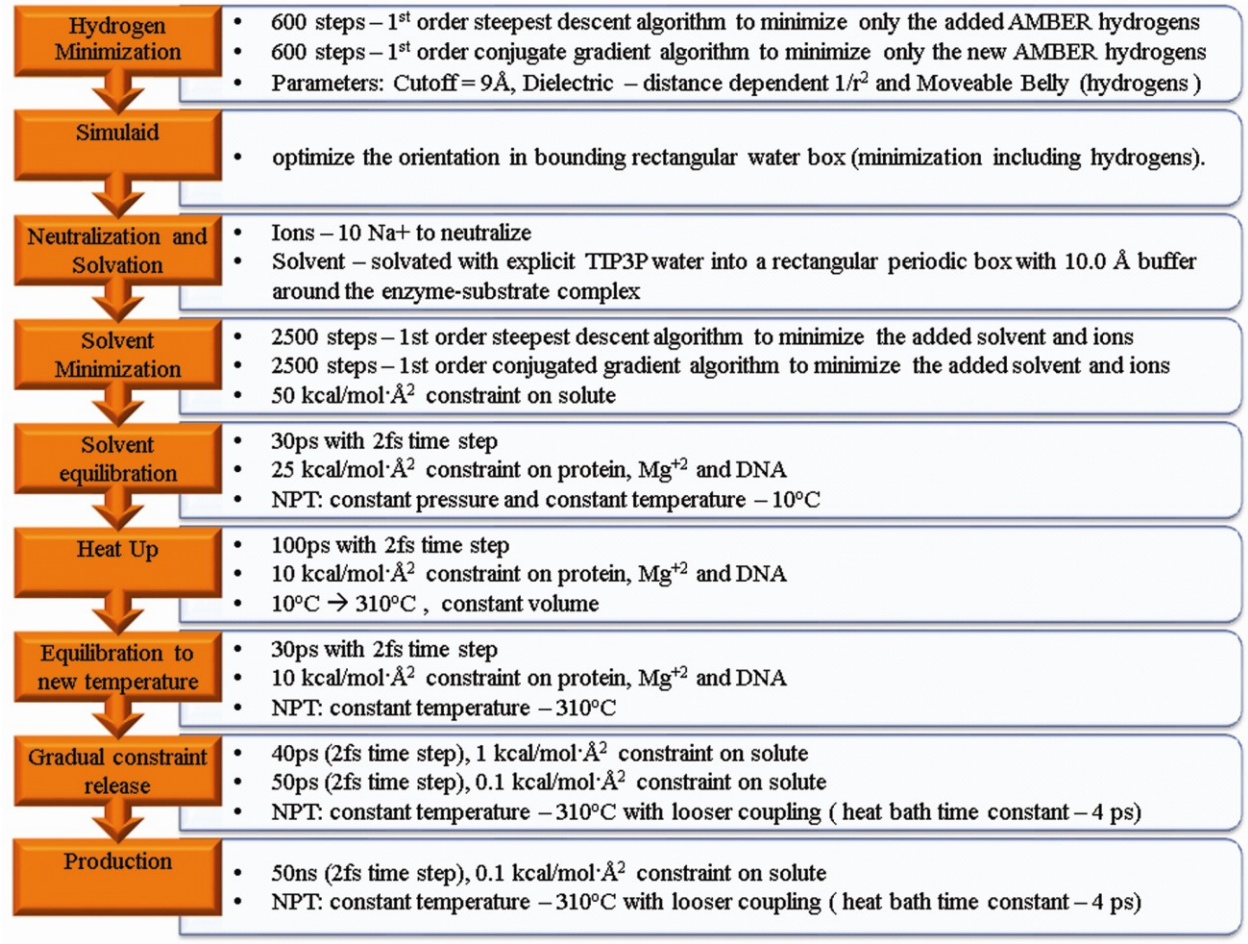

Scheme S1. MD protocol

SUPPLEMENTAL FIGURES

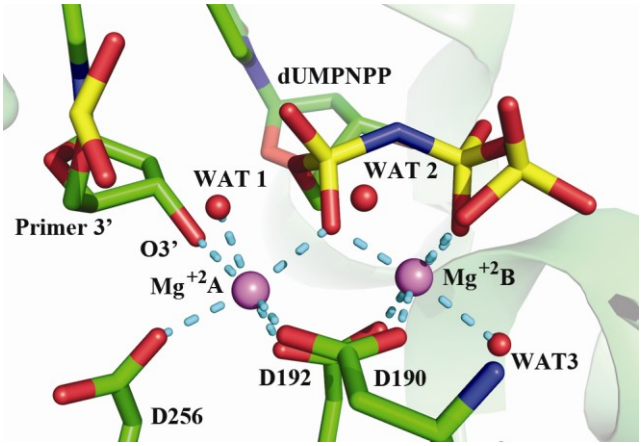

Figure S1. Pol β active site (PDB ID: 2FMS (34)). A second crystal water is located at the active site in a similar position as the solvent water in our model.

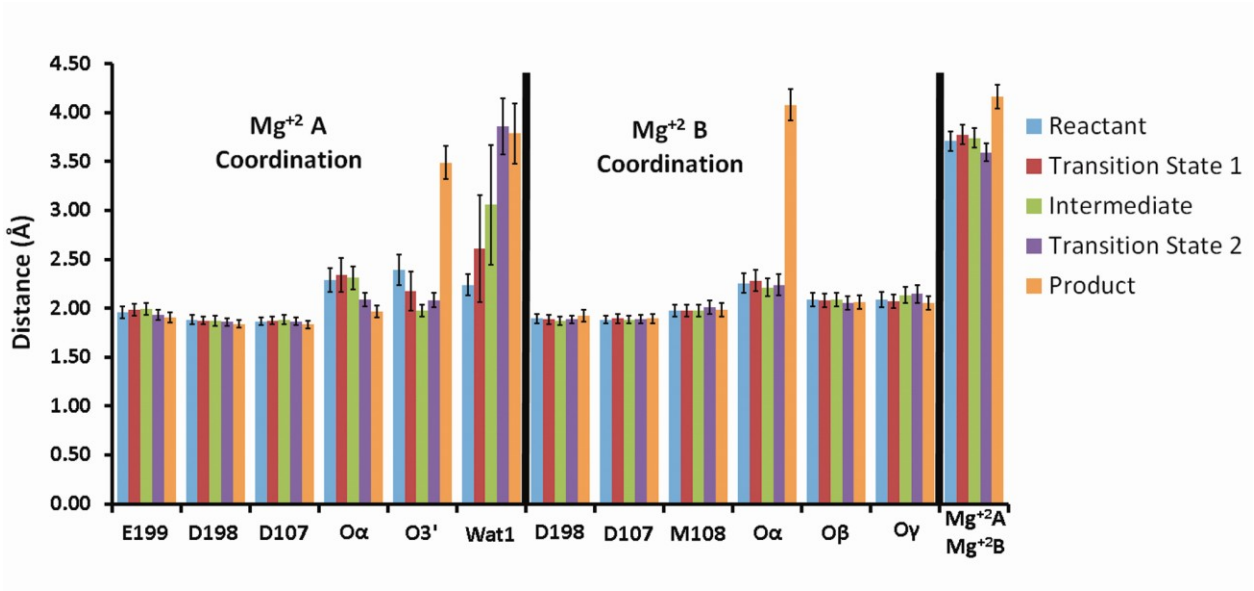

Figure S2. Ensemble average coordination distances of Mg^{+2} A and Mg^{+2} B and inter-magnesium ion distance at stationary points along the reaction coordinate with standard deviations. The distance between the catalytic Mg^{+2} A and the nucleotide binding Mg^{+2} B becomes shorter and achieves a minimum at the transition state, and it subsequently elongates again to facilitate the breaking of the P_{α}–$O_{\alpha,\beta\text{-bridge}}$ bond.

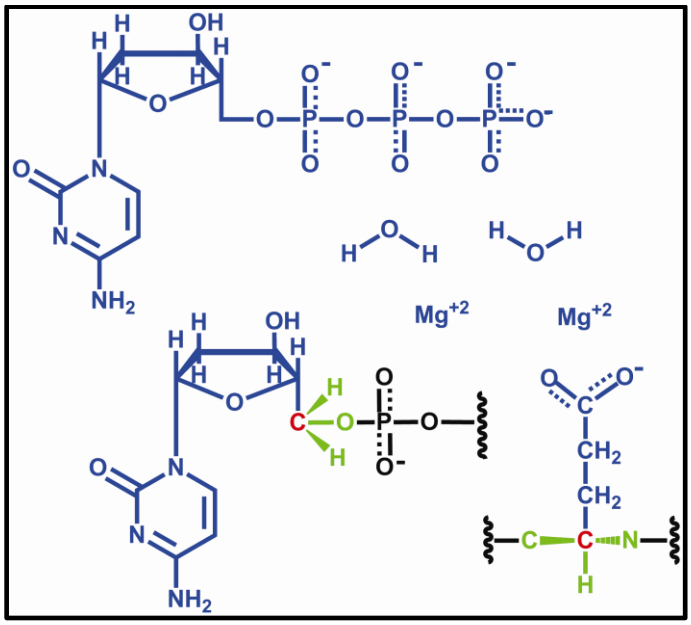

Figure S3. Division of the QM/MM system. The system is partitioned into QM and MM subsystems. In the active site region, the QM subsystem (colored in blue) comprises the dCTP, the primer 3'-nucleotide (excluding the C5' phosphate group), the catalytic glutamic acid (E199), the nucleotide-binding and catalytic Mg^{+2} ions, and two water molecules. The pseudobonds are the C5' atom of the primer 3'- nucleotide and C_α of E199 (colored in red). The two O5' atoms (colored in green) which are directly connected to the pseudobond C5' are set to have zero point charge. The atoms C_α, H and N (also colored in green), connected to the pseudobond C_α, also have zero point charge assigned. All other atoms belong to the MM subsystem (colored in black).

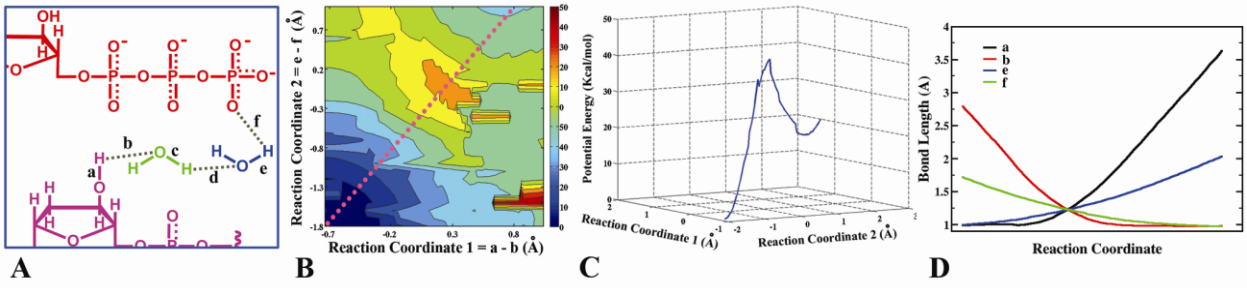

Figure S4. Hydrogen shuttle step of the WMSA mechanism at the QM/MM calculation stage: (A) Mechanistic scheme of the three hydrogen transfers; a, c and e indicate the breaking O–H bonds, b, d and f indicate the forming O–H bonds. (B) Two dimensional potential energy surface. Reaction coordinate 1 is the hydrogen transfer from O3' to WAT1; Reaction coordinate

2 is the hydrogen transfer from WAT2 to the γ-phosphate. The transfer from WAT1 to WAT2 is not driven. (C) The two dimensional potential energy profile corresponds to the pink line in (B). (D) Concerted hydrogen shuttling shown from bond length analysis.

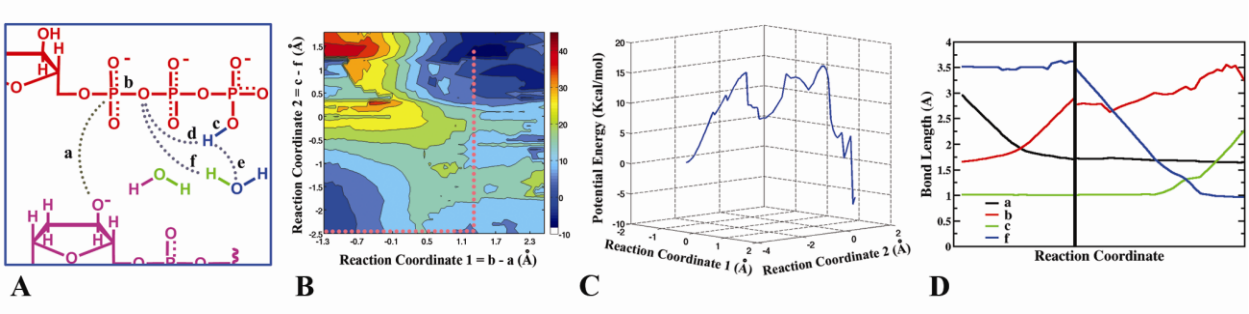

Figure S5. Nucleophilic attack step of the WMSA mechanism at the QM/MM calculation stage: (A) Mechanistic scheme of the nucleophilic attack (a and b) and possible hydrogen transfers from the γ-phosphate to the α,β-bridging oxygen (directly, c and d; via a water e and f). (B) Two dimensional potential energy surface Reaction coordinate 1 is the phosphoryl transfer; Reaction coordinate 2 is the hydrogen transfer from the γ-phosphate to the α,β-bridge via WAT2. (C) The two dimensional potential energy profile corresponds to the pink dotted path in (B). (D) Bond analysis. The left side of the plot is the phosphoryl transfer that corresponds to the horizontal line in (B), the O3'–P_α (black) becomes shorter while the P_α–$O_{\alpha,\beta\text{-bridge}}$ bond (red) becomes longer. The right side is the hydrogen transfer through a water that corresponds to the vertical line in (B), in which the hydrogen returns to the water (blue) and a hydrogen from the water goes to the $O_{\alpha,\beta\text{-bridge}}$ (green). The PMF in the main text Figure 3 is the path represented by the horizontal line in (B) while the hydrogen transfer to the α,β-bridging oxygen occurs spontaneously and without the mediating water (described as path c,d in (A)), during the QM/MM-MD simulation of the horizontal line path.

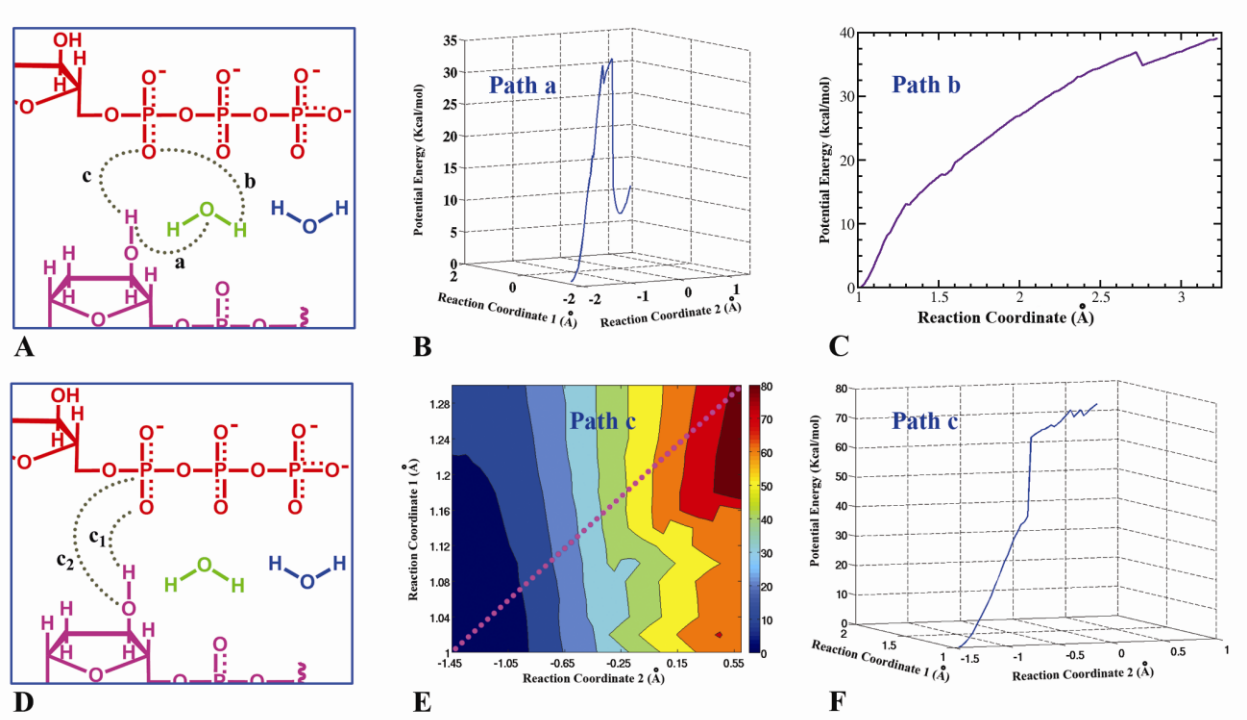

Figure S6. Mechanisms involving proton transfer from H(O3') to the α-phosphate, starting from the reactant with the H(O3') directed towards the α-phosphate of the dCTP (see Figure 8, main text). (A) Mechanistic scheme of hydrogen transfer from the O3' to the α-phosphate oxygen via a mediating water (path a) and of direct transfer (path b). (B) Energy profile of path a. (C) Energy profile of path b. In both paths a and b, upon a short unrestrained QM/MM-MD the hydrogen went back to the primer O3' to produce the reactant structure. (D) Mechanistic scheme of direct hydrogen transfer from the O3' to the α-phosphate oxygen simultaneously with the nucleophilic attack (path c). In (E) we show the two dimensional potential energy surface in which one reaction coordinate allows release of the H(O3') by elongation of the O3'-H bond (c_1 in (D) and RC1 in (E) and (F)), while in the second reaction coordinate we drive the nucleophilic attack (c_2 in (D) and RC2 in (E) and (F)). While the phosphoryl transfer progresses, the released hydrogen is transferred to the α-phosphate, but the energy was very high and only uphill as shown in (F) which is the dotted diagonal of (E).

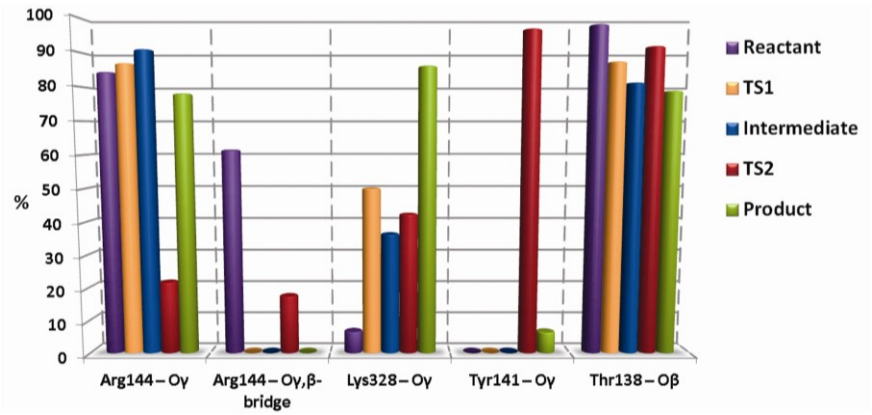

Figure S7. Hydrogen bond occupancies involving incoming dCTP and active site residues.

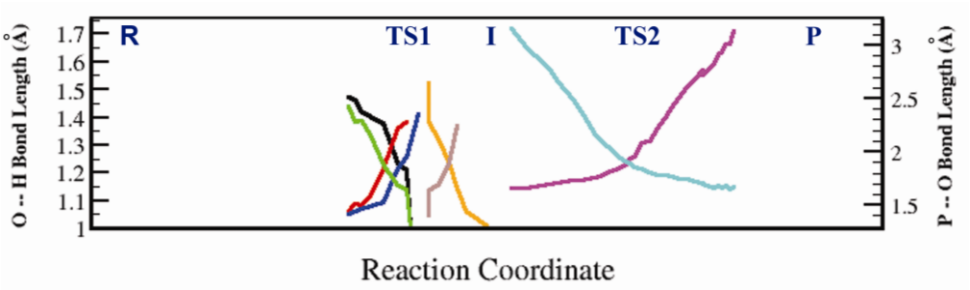

Figure S8. Bond breakage and formation: the green-red cross describes the first hydrogen transfer from O3' to the crystal Wat1; the black-blue cross is the second hydrogen transfer from Wat1 to solvent Wat2; the orange-brown cross is the hydrogen transfer from Wat2 to the γ-phosphate, and the cyan-magenta cross is the breakage and formation of the P_α-O bond and the O3'-P_α bond, respectively. See Figure 3 in the main text.

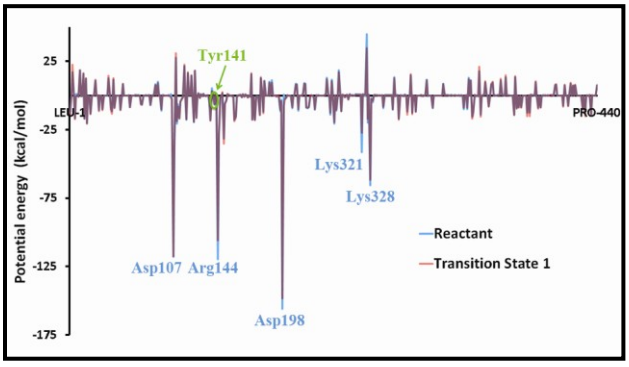

Figure S9. Stabilizing interactions (electrostatic and van der Waals) between Pol κ amino acid residues and the QM active site region (defined in Figure S3) for the Reactant and the first Transition State (Figure 4 in the main text).

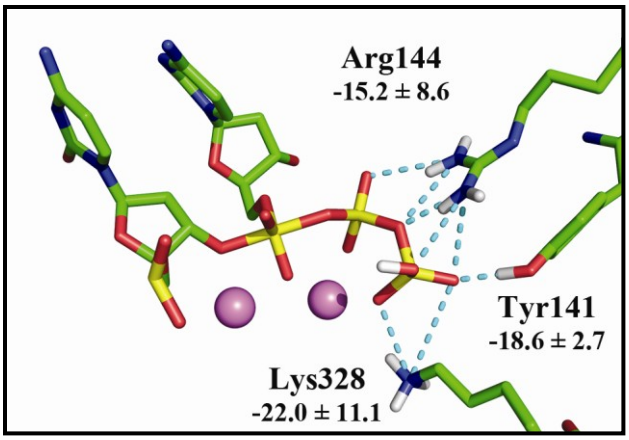

Figure S10. Stabilizing interactions between Pol κ amino acid residues and the QM active site region (defined in Figure S3). The electrostatic and van der Waals interactions between Pol κ amino acid residues of the MM region and the QM region (see Figure S3) were calculated for the Intermediate and Transition State 2 (see Figure 4 in the main text) over the last 10 ps (1000 snapshots) of QM/MM-MD simulation, and the difference between them is shown. This difference emphasizes the added stabilization that these three residues provide at the transition state.

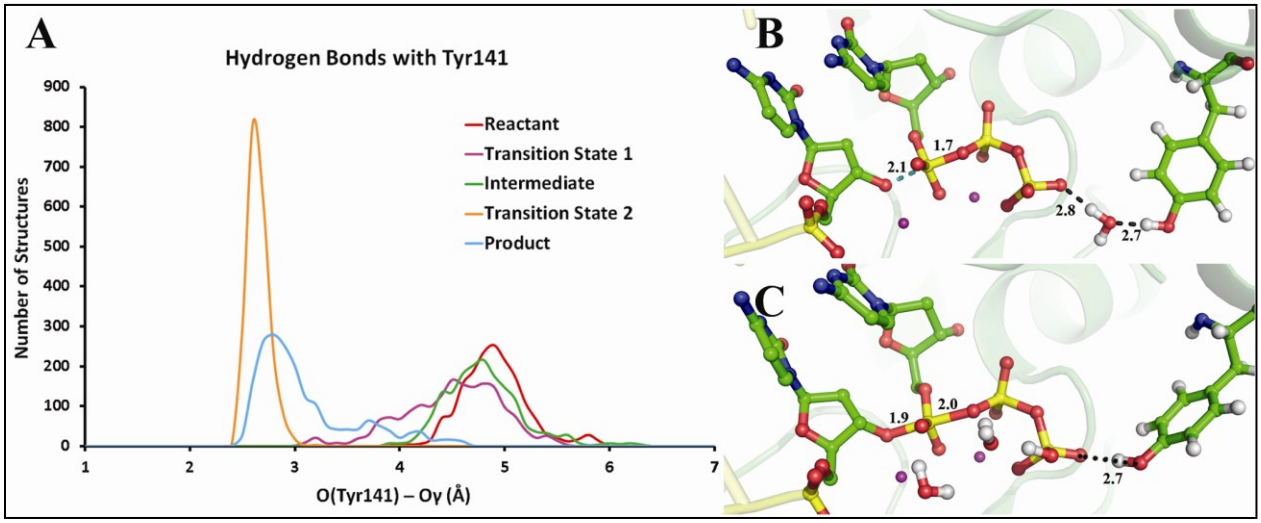

Figure S11. Interaction of Tyr141 with the γ-phosphate either directly or through water. (A) Distribution of $O_{(Tyr141)} - O\gamma_{(dCTP)}$ distances. The data was collected from the last 10 ps (1000 snapshots) of QM/MM-MD simulation. Representative structures of the active site with Tyr141 hydrogen bonded to Oγ of dCTP via a water in (B) Reactant and (C) Transition State 2.

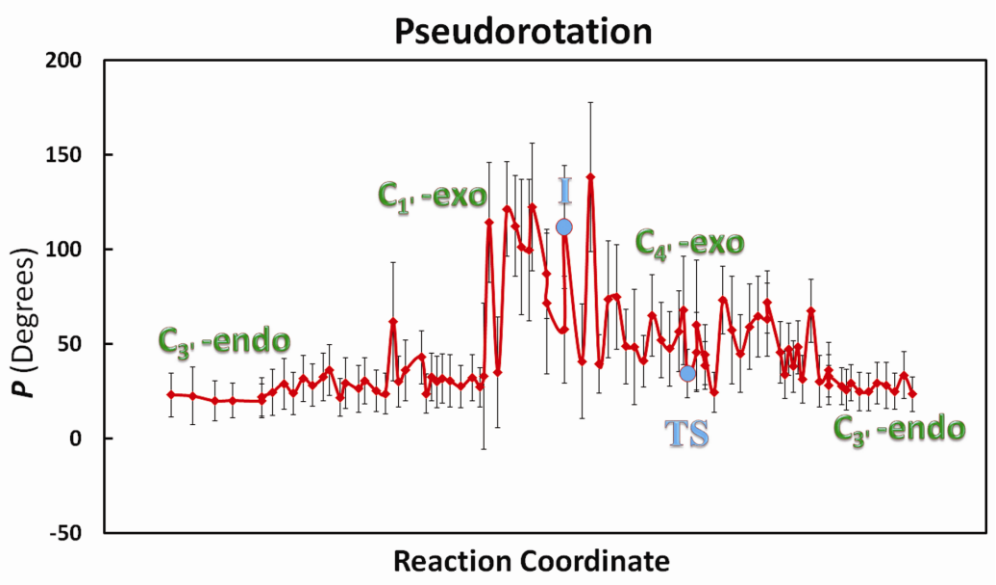

Figure S12. Sugar pucker pseudorotation parameter ***P*** as a function of the reaction coordinate with Intermediate (I) and pentacovalent phosphorane transition state (TS) designated.

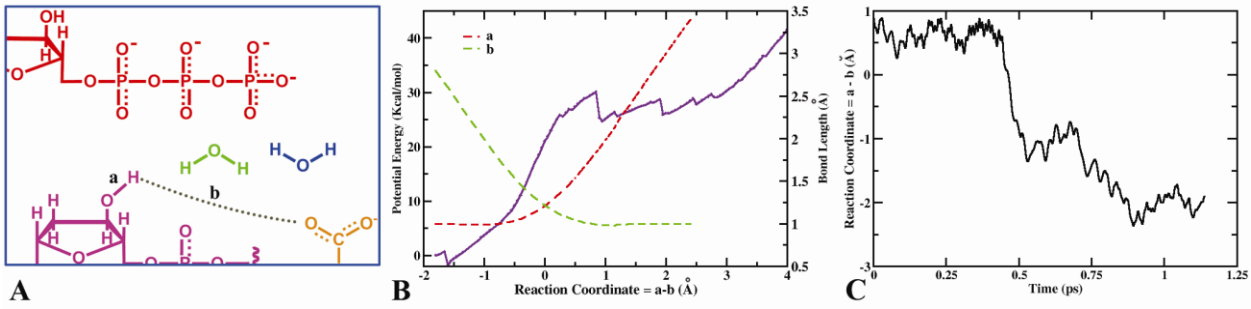

Figure S13. E199 as the general base for H(O3') utilizing a stepwise mechanism in which the O3' is deprotonated before the nucleophilic attack. This always resulted in an uphill energy profile and produced an unstable intermediate that upon short unrestrained QM/MM-MD converged back to the reactant structure. (A) The mechanism scheme. (B) Potential energy profile of the O3' deprotonation. (C) A short unrestrained QM/MM-MD simulation shows that the system returns to the reactant structure.

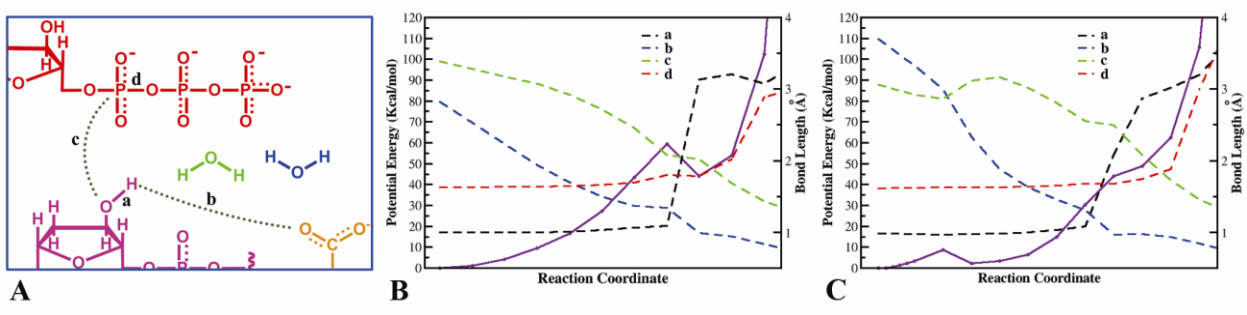

Figure S14. Mechanism with E199 as the general base for the H(O3') with a one-step mechanism for the O3' deprotonation and the nucleophilic attack. This always resulted in an uphill energy profile and produced an unstable intermediate that upon a short unrestrained QM/MM-MD converged back to the reactant structure. (A) The mechanism scheme. (B) Path that starts from the reactant with the H(O3') directed towards E199. (C) Path that starts from the reactant with the H(O3') directed towards the α-phosphate of the dCTP (see Figure 8, main text).

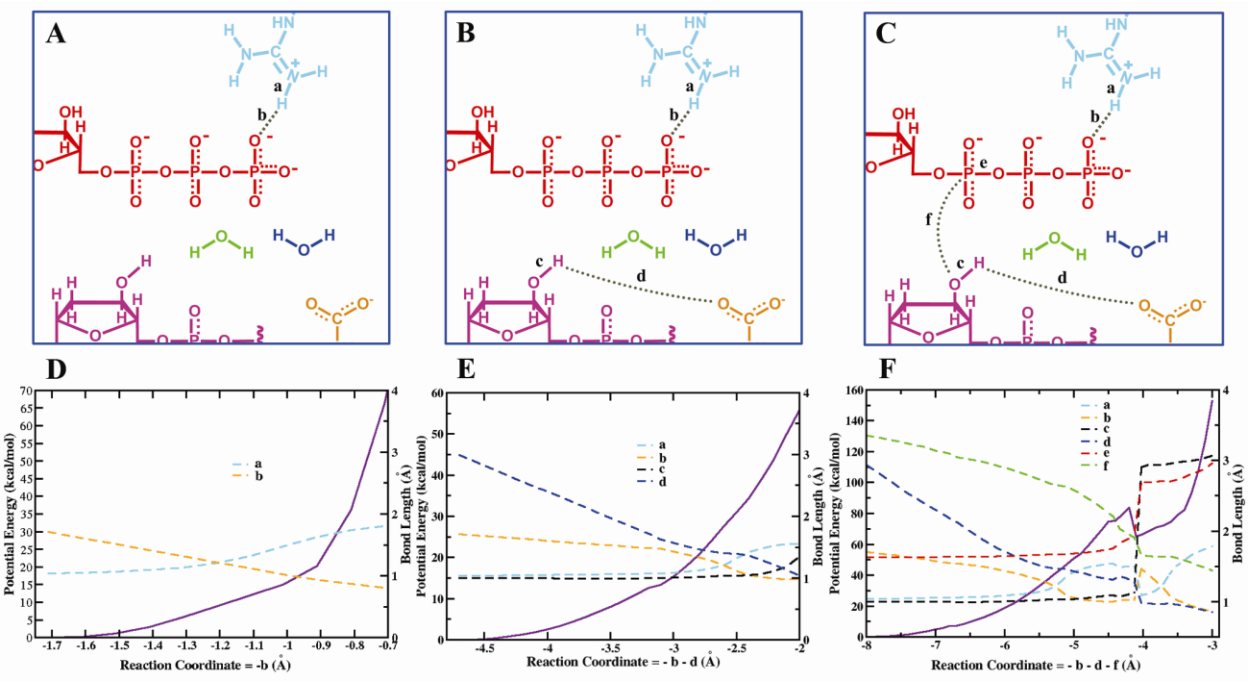

Figure S15. Potential energies and mechanism schemes involving Arg144: (A) Path that involves protonation of the γ-phosphate by Arg144. (B) Path that combines proton donation by Arg144 with E199 serving as the base for the H(O3'). (C) Same as (B) except that the nucleophilic attack is simultaneous with the proton transfers. For (C) in the TS of the nucleophilic attack, the H(O3') transferred to E199, but the proton that was transferred to the γ-

phosphate from Arg144 returned back to this amino acid, producing an uphill energy profile. (D-F) Potential energy profiles with bond length analysis to (A-C) schemes respectively.

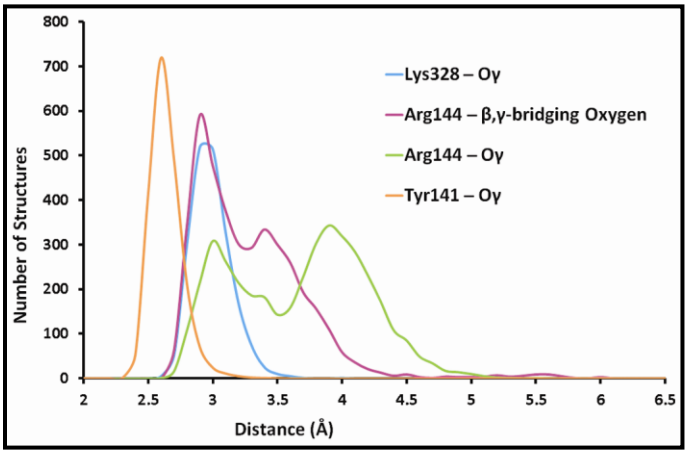

Figure S16. Hydrogen bonding interactions are preserved in the pentacovalent phosphorane transition state for the B[*a*]P modified system as for the unmodified system; this is shown by the population distribution of $O_{(dCTP)}$–$O_{(donor\ residue)}$ distances (Å) between key active site residues and dCTP in the B[*a*]P modified system at the pentacovalent phosphorane transition state. Arg144 dynamically utilized multiple hydrogen bonding opportunities with the γ-phosphate oxygens and with the β,γ-bridging oxygen at times in alternation (see Figure 5B in the main text); thus the Arg144 histograms contain two peaks.

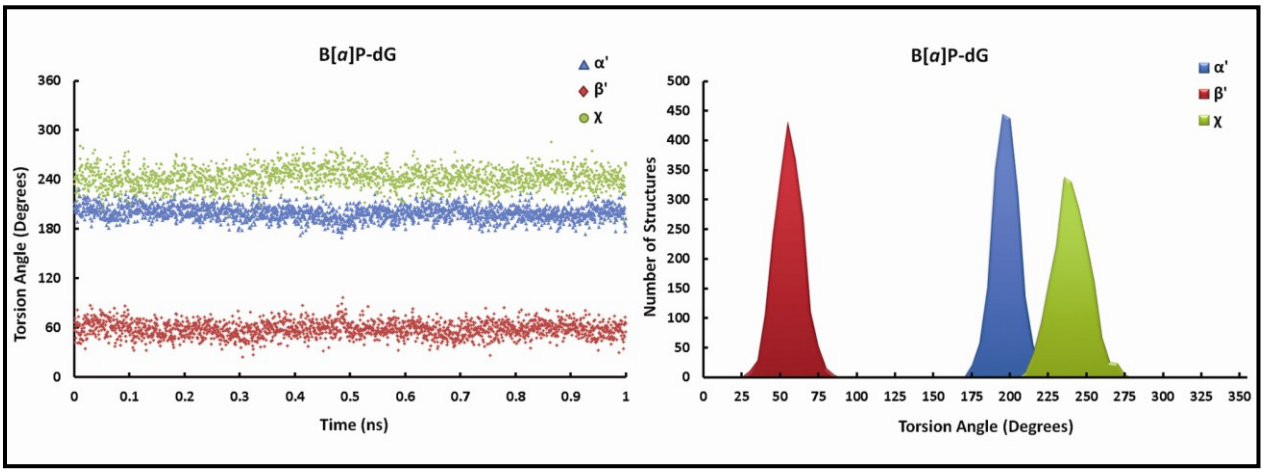

Figure S17. Torsion angles of the 10*S* (+)-*trans*-*anti*-B[*a*]P-N^2-dG (B[*a*]P-dG) adduct at the modified system transition state 2 (see structure in Figure 5B, Figure 9 and Figure 10 B in the main text). Torsion angles are defined as χ = O4'(dR) – C1'(dR) – N9 – C4 (dR is deoxyribose),

α'= N1– C2–N^2 – C10(B[*a*]P-dG) , β'= C2–N^2– C10(B[*a*]P-dG) – C9(B[*a*]P-dG) as shown in Figure 1 in the main text.

SUPPLEMENTAL MOVIES

Movie S1. Shuttling of the O3' proton through waters to the γ-phosphate.

Movie S2. Nucleophilic attack of O3' on α–phosphate, formation of the pentacovalent phosphorane transition state, proton transfer from γ–phosphate to α,β-bridge and leaving of pyrophosphate.

Movie S3. Pol κ containing the B[*a*]P-dG lesion at the pentacovalent phosphorane transition state during the nucleophilic attack. The pentacovalent phosphorane is designated by an asterisk.

SUPPLEMENTAL TABLES

Force Field Parameters for the Pentacovalent Phosphorane

Table S1: Topology assignments and partial charges for the pentacovalent phosphorane transition state. Partial charges were taken from the QM/MM calculation.

Atom	Atom Type	Connection Type	Partial Charge
P	P	M	1.166
O1P	O2	E	-0.776
O2P	O2	E	-0.776
O0*	OS	M	-0.495
C0*	CT	M	-0.007
1H0	H1	E	0.075
2H0	H1	E	0.075
C9*	CT	M	-0.977
H9*	H1	E	0.317
O9*	OS	M	-0.235
C6*	CT	M	0.466
H6*	H2	E	0.090
N5	N*	S	-0.704
C9	CM	B	0.443
H9	H4	E	0.005
C8	CM	B	-0.796
H8	HA	E	0.249
C7	CA	B	1.163
N7	N2	B	-1.047
H71	H	E	0.483
H72	H	E	0.491

N6	NC	S	-1.066
C1	C	S	1.183
O1	O	E	-0.764
C7*	CT	M	-0.107
1H7	HC	E	-0.006
2H7	HC	E	0.056
C8*	CT	M	0.873
H8*	H1	E	-0.058
O8*	TO	M	-1.118
PA	TP	M	1.488
O1A	O2	E	-1.013
O2A	O2	E	-0.786
O3A	TO	S	-0.828
PB	P	3	1.490
O1B	O2	E	-0.863
O2B	O2	E	-0.951
O3B	OS	S	-0.627
PG	P	3	1.169
O1G	GO	S	-0.888
GH	GH	E	0.461
O2G	O2	E	-0.763
O3G	O2	E	-0.956
O5*	OS	M	-0.193
C5*	CT	M	-0.434
1H5	H1	E	0.198
2H5	H1	E	0.151
C4*	CT	M	0.422
H4*	H1	E	-0.026
C3*	CT	3	0.378
H3*	H1	E	0.122
C2*	CT	B	-0.362
1H2	HC	E	0.130
2H2	HC	E	0.087
O3*	OH	S	-0.726
H3T	HO	E	0.419
O4*	OS	M	-0.446
C1*	CT	M	0.248
H1*	H2	E	0.102
N1	N*	M	-0.292
C6	CM	M	0.350
H6	H4	E	0.023
C5	CM	M	-0.737
H5	HA	E	0.240

C4	CA	M	1.057
N4	N2	B	-1.028
H41	H	E	0.478
H42	H	E	0.464
N3	NC	M	-0.995
C2	C	S	0.987
O2	O	E	-0.786

Table S2. Geometrical parameters for the transition state were characterized by QM/MM-MD calculations and were added to the Parm99SB.dat parameter set

Bond Parameters		
AMBER Bond Type	Harmonic Force Constant k_r (kcal $mol^{-1}Å^{-2}$)	Equilibrium Bond Length r_{eq} (Å)
O2 - TP	525	1.48
OS - TP	460	1.61
TO - TP	1000	1.9
TO - CT	640	1.41
TO - P	460	1.61
GH - GO	553	0.96
GO - P	460	1.61

Angle Parameters		
AMBER Angle Type	Harmonic force constant K_q (kcal mol^{-1} rad^{-2})	Equilibrium Angle q_{eq} (^{o})
TO-TP-TO	600	175.3
CT-TO-TP	300	120.7
CT-OS-TP	500	118.0
P -TO-TP	300	131.6
OS-TP-TO	200	90.0
TO-TP-O2	200	90.0
OS-TP-O2	200	120.0
O2-TP-O2	300	120.0
TO-P -O2	100	112.5
TO-P -OS	100	99.0
TO-CT-CT	100	112.9
TO-CT-H1	150	103.8
GH-GO-P	200	112.2

GO-P -O2	100	108.2
GO-P -OS	100	102.6

Torsion Parameters			
AMBER Torsion type	Torsion Barrier $V_n/2$ (kcal/mol)	Phase Angle $\gamma(^o)$	Periodicity *n*
OS-TP-TO-CT	0.250	0	-3
OS-TP-TO-CT	1.200	0	2
TO-TP-TO-CT	0.250	0	-3
TO-TP-TO-CT	1.200	0	2
P -TO-TP-TO	0.250	0	3
P -TO-TP-O2	0.250	0	3
P -TO-TP-OS	0.250	0	3
CT-TO-TP-O2	0.250	0	3
TP-TO-P -O2	0.250	0	3
TP-TO-P -OS	0.250	0	3
CT-CT-TO-TP	0.380	0	3
H1-CT-TO-TP	0.380	0	3
CT-OS-TP-O2	0.250	0	3
TO-TP-OS-CT	0.250	0	-3
TO-TP-OS-CT	1.200	0	2
P -OS-P -TO	0.250	0	3
HC-CT-CT-TO	0.250	0	1
TO-CT-CT-CT	0.150	0	3
TO-CT-CT-OS	0.144	0	-3
TO-CT-CT-OS	1.175	0	2
GH-GO-P -O2	0.250	0	3
GH-GO-P -OS	0.250	0	3
GO-P -OS-P	0.250	0	3

Pentacovalent Phosphorane Structure

Table S3. Active site properties at the pentacovalent phosphorane transition state.

Distance	Unmodified DNA system using QM/MM-MD simulations (Å)	Unmodified DNA system using MD simulations (Å)	Modified DNA system using MD simulations (Å)
O3'-P_α	1.85 ± 0.04	1.88 ± 0.02	1.88 ± 0.02
P_α-$O_{\alpha,\beta\text{-bridging}}$	1.95 ± 0.05	1.87 ± 0.02	1.87 ± 0.02
Mg^{+2} A – Mg^{+2} B	3.59 ± 0.09	3.40 ± 0.07	3.42 ± 0.07
Mg^{+2} A – E199	1.93 ± 0.05	1.88 ± 0.04	1.88 ± 0.05

Mg^{+2} A – D198	1.86 ± 0.04	1.93 ± 0.06	1.91 ± 0.05
Mg^{+2} A – D107	1.86 ± 0.04	1.89 ± 0.05	1.90 ± 0.05
Mg^{+2} A – O_α	2.09 ± 0.07	1.96 ± 0.06	1.97 ± 0.06
Mg^{+2} A – O3'	2.08 ± 0.07	1.82 ± 0.03	1.82 ± 0.03
Mg^{+2} A – WAT*	3.86 ± 0.29	3.55 ± 1.24	2.26 ± 0.35
Mg^{+2} B – M108	2.01 ± 0.07	2.13 ± 0.11	2.15 ± 0.11
Mg^{+2} B – D107	1.89 ± 0.04	1.91 ± 0.05	1.90 ± 0.05
Mg^{+2} B – D198	1.89 ± 0.04	1.91 ± 0.05	1.92 ± 0.05
Mg^{+2} B – O_α	2.24 ± 0.11	1.98 ± 0.07	1.97 ± 0.07
Mg^{+2} B – O_β	2.05 ± 0.07	1.87 ± 0.04	1.87 ± 0.04
Mg^{+2} B – O_γ	2.15 ± 0.09	1.88± 0.05	1.88 ± 0.05
Lys328 – O_γ	2.86 ± 0.10	2.93 ± 0.15	3.04 ± 0.15
Tyr141 – O_γ	2.70 ± 0.11	2.72 ± 0.18	2.69 ± 0.12
Thr138 – O_β	2.72 ± 0.11	2.67 ± 0.11	2.71 ± 0.12

REFERENCES

30. Jia, L., Geacintov, N.E. and Broyde, S. (2008) The N-clasp of human DNA polymerase kappa promotes blockage or error-free bypass of adenine- or guanine-benzo[a]pyrenyl lesions. *Nucleic Acids Res*, **36**, 6571-6584.
32. Lone, S., Townson, S.A., Uljon, S.N., Johnson, R.E., Brahma, A., Nair, D.T., Prakash, S., Prakash, L. and Aggarwal, A.K. (2007) Human DNA polymerase kappa encircles DNA: implications for mismatch extension and lesion bypass. *Mol Cell*, **25**, 601-614.
34. Batra, V.K., Beard, W.A., Shock, D.D., Krahn, J.M., Pedersen, L.C. and Wilson, S.H. (2006) Magnesium-induced assembly of a complete DNA polymerase catalytic complex. *Structure*, **14**, 757-766.
46. Berman, H.M., Battistuz, T., Bhat, T.N., Bluhm, W.F., Bourne, P.E., Burkhardt, K., Feng, Z., Gilliland, G.L., Iype, L., Jain, S. *et al.* (2002) The Protein Data Bank. *Acta Crystallogr., Sect D: Biol. Crystallogr.*, **58**, 899-907.
47. D.A. Case, T.A.D., T.E. Cheatham, III, C.L. Simmerling, J. Wang, R.E. Duke, R. Luo, K.M. Merz, D.A. Pearlman, M. Crowley, R.C. Walker, W. Zhang, B. Wang, S. Hayik, A. Roitberg, G. Seabra, K.F. Wong, F. Paesani, X. Wu, S. Brozell, V. Tsui, H. Gohlke, L. Yang, C. Tan, J. Mongan, V. Hornak, G. Cui, P. Beroza, D.H. Mathews, C. Schafmeister, W.S. Ross, and P.A. Kollman. (2006). 9.0 ed. University of California, San Francisco.
54. Price, D.J. and Brooks, C.L., 3rd. (2004) A modified TIP3P water potential for simulation with Ewald summation. *J Chem Phys*, **121**, 10096-10103.
65. Ling, H., Sayer, J.M., Plosky, B.S., Yagi, H., Boudsocq, F., Woodgate, R., Jerina, D.M. and Yang, W. (2004) Crystal structure of a benzo[a]pyrene diol epoxide adduct in a ternary complex with a DNA polymerase. *Proc Natl Acad Sci U S A*, **101**, 2265-2269.
89. Uljon, S.N., Johnson, R.E., Edwards, T.A., Prakash, S., Prakash, L. and Aggarwal, A.K. (2004) Crystal structure of the catalytic core of human DNA polymerase kappa. *Structure*, **12**, 1395-1404.
90. Gordon, J.C., Myers, J.B., Folta, T., Shoja, V., Heath, L.S. and Onufriev, A. (2005) H++: a server for estimating pKas and adding missing hydrogens to macromolecules. *Nucleic Acids Res*, **33**, W368-371.

91. Anandakrishnan, R. and Onufriev, A. (2008) Analysis of basic clustering algorithms for numerical estimation of statistical averages in biomolecules. *J Comput Biol*, **15**, 165-184.
92. Dolinsky, T.J., Nielsen, J.E., McCammon, J.A. and Baker, N.A. (2004) PDB2PQR: an automated pipeline for the setup of Poisson-Boltzmann electrostatics calculations. *Nucleic Acids Res*, **32**, W665-667.
93. Mezei, M. (2003) A new method for mapping macromolecular topography. *Journal of molecular graphics & modelling*, **21**, 463-472.
94. Darden, T.Y., D.; Pedersen, L. . (1993.) Particle mesh Ewald: an NlogN method for Ewald sums in large systems. . *J. Chem. Phys.*, **98**, 10089–10092.
95. Essmann, U.P., L.; Berkowitz, M. L.; Darden, T.; Lee, H.; Pedersen, L. (1995) A smooth particle mesh Ewald method. . *J. Chem. Phys.* , **103**, 8577–8593.
96. Ryckaert, J.P.C., G.; Berendsen, H. J. . (1977) Numerical integration of the cartesian equations of motion of a system with constraints: molecular dynamics of n-alkanes. *J. Comput. Phys.*, **23**, 327–341.
97. Berendsen, H.J.C., Postma, J.P.M., van Gunsteren, W.F., DiNola, A. and Haak, J.R. (1984) Molecular dynamics with coupling to an external bath. *J. Chem. Phys.*, **81**, 3684-3690.